 doi:10.20944/preprints201701.0063.v1

Crystal Structure and Physical Properties of HfB_4 via First-Principles Calculations

Gangtai Zhang [1], Rui Gao [2], Yaru Zhao [1], Tingting Bai [3] and Yanfei Hu [4,*]

[1] College of Physics and Optoelectronics Technology, Baoji University of Arts and Sciences, Baoji 721016, China; gtzhang79@163.com (G.Z.); scu_zyr@163.com (Y.Z.)

[2] College of Electrical and Electronic Engineering, Baoji University of Arts and Sciences, Baoji 721016, China; gaorui262@sohu.com (R.G.)

[3] College of Mathematics and Information Science, Baoji University of Arts and Sciences, Baoji 721013, China; btt1120@163.com (T.B.)

[4] School of Science, Sichuan University of Science and Engineering, Zigong 643000, China

* Correspondence: yanfei_hu1982@suse.edu.cn (Y.H.); Tel.: +86-813-550-5662

Abstract: By using the particle swarm optimization algorithm for crystal structure prediction, we reveal a newly orthorhombic *Cmcm* structure of HfB_4, which is more energetically superior to the previously proposed YB_4-, ReP_4-, FeB_4-, CrB_4-, and MnB_4-type structures in the considered pressure range. The phonon dispersion and elastic constants calculations confirm that the new phase is dynamically and mechanically stable. The calculated large shear modulus (240 GPa) and high hardness (45.7 GPa) imply that the predicted *Cmcm*-HfB_4 is a potential superhard material. Meanwhile, the directional dependences of the Young's modulus, bulk modulus, and shear modulus for HfB_4 are systematically investigated. Further analyses of the density of states and electronic localization function indicate that the strong B-B and B-Hf covalent bonds greatly contribute to its high hardness and stability.

Keywords: HfB_4; structure prediction; superhard material; anisotropic properties

PACS: 61.66.Fn; 61.50.Ah; 62.20.de

1. Introduction

Incompressible and superhard materials are very useful in a variety of industrial applications, such as cutting and polishing tools, abrasives, oil exploitations, wear-resistant coatings. Thus intense scientific interests have been devoted to synthesizing and designing superhard materials. Currently, there are two kinds of materials that are deemed to be potential

Preprints (www.preprints.org) | NOT PEER-REVIEWED | Posted: 12 January 2017 doi:10.20944/preprints201701.0063.v1

candidates for superhard materials. The first one is the strongly three-dimensional covalent bonded compounds formed by light elements B, C, N, and O, such as diamond [1], *c*-BN [2], B_6O [3], BC_2N [4] etc. Unfortunately, all these superhard materials are expensive and exiguous because they either occur naturally in limited supplies or have to be synthesized only at high-temperature and high-pressure conditions. The second one is by combining heavy transition metal (TM) atoms with light atoms (B, C, N, and O). In this case, the compounds formed by TMs and light atoms usually hold high valence electron density and directional covalent bonds, and these covalent bonds are strong enough to improve the mechanical properties and create high hardness. On the other hand, *d* valence electrons are also considered to contribute to the hardness of TM compounds. According to this design criterion, many TM borides have been synthesized, such as ReB_2 [5], OsB_2 [6], RuB_2 [7], YB_4 [8], MnB_4 [9-11], FeB_4 [12], CrB_4 [13,14] and son on. Also, WB_4 with a hexagonal structure ($P6_3/mmc$, $Z = 4$) was synthesized at ambient pressure and was proposed to be a potential superhard material with the claimed hardness of 31.8-46.2 GPa [15]. However, the later studied results have shown that the hexagonal WB_4 phase is instable and it is actually WB_3 with a MoB_3-type structure [16-19]. Theoretically, based on the crystal structure search code and first-principles calculations, the structure and physical properties of boron-rich TM (TM=Ti, V, Mn, Zr, Nb, Mo, Tc, Ta, W, Re, Os, and Ir) compounds have been extensively investigated [20-30]. The obtained results showed that these materials possess high bulk and shear moduli. In addition to that, TM borides can be synthesized under ambient pressure, which reduces the cost of the synthesis and is benefit for their application. So TM borides are good candidates as hard or superhard materials.

In a survey of the Hf-B system, we found that three known binary structures [31], namely HfB, HfB_2, and HfB_{12}, have been synthesized experimentally. HfB with a NaCl-type structure was obtained from the hot-pressing of equal amounts of Hf and B in graphite dies and subsequent heat treatment at 1400 °C [31]. For each NaCl-type HfB unit cell, it contains four HfB formula units, in which B atom occupies the Wyckoff 4*b* (0.5, 0.5, 0.5) sites and Hf atom situates 4*a*-sites at origin. Several studies [31-33] also suggested that HfB has an orthorhombic FeB structure and its thermal stability is in the temperature region of $1200 < T < 2000$ °C. HfB_2 belongs to a hexagonal AlB_2 structure with a space group symmetry $P6/mmm$ [31], for its high

Preprints (www.preprints.org) | NOT PEER-REVIEWED | Posted: 12 January 2017 doi:10.20944/preprints201701.0063.v1

physico-mechanical characteristics and capability of maintaining thermodynamic characteristics at elevated temperatures (T=3350°C) [34], HfB_2 is one of the most promising candidates for protection materials. Additionally, HfB_2 ceramics exhibit many unique properties, such as high melting temperature, high hardness, low electrical resistivity, and high chemical stability, the combination of these properties make them potential candidates for various high-temperature structural applications. HfB_{12} with a cubic UB_{12} structure was experimentally synthesized by a mixture of Hf and B at 6.5 GPa and 1600-2100°C [35]. Nevertheless, the attempts to synthesize HfB_{12} at ambient pressure have proved to be unsuccessful [35,36]. Hence, this synthesized UB_{12}-type HfB_{12} is a metastable phase. Recently, an experimental study showed that the high-pressure cubic HfB_{12} phase can be successfully stabilized in the $Y_{1-x}Hf_xB_{12}$ system under ambient pressure [37]. Furthermore, the crystal structure and related physical properties of HfB, HfB_2, and HfB_{12} have been widely investigated [38-48]. However, there is no experimental report on the synthesis of hafnium tetraborides; besides, the theoretical research works of hafnium tetraborides are also seldom up to now.

In the present work, we have extensively explored the crystal structures of HfB_4 by using the particle swarm optimization (PSO) algorithm for crystal structure prediction [49-51], which only requires the chemical compositions for a given compound at specified external conditions, unbiased by any known information. An orthorhombic *Cmcm* structure is predicted for HfB_4, which is energetically much more preferable than the earlier proposed YB_4-, ReP_4-, FeB_4-, CrB_4-, and MnB_4-type structures in the pressure range of 0-50 GPa. First principles calculations are then performed to investigate the total energy, lattice parameters, phonon, formation enthalpy, mechanical properties, density of states, and chemical bonding character for this novel orthorhombic phase. In addition, other hafnium borides with various stoichiometries are also studied for comparison.

2. Computational methods

To determine the stable crystal structure of HfB_4, the PSO methodology on the crystal structure analysis by the particle swarm optimization (CALYPSO) code [52] is employed at 0 GPa with 1-4 formula units (f.u.) in the simulation cell. The underlying *ab initio* structural

Preprints (www.preprints.org) | NOT PEER-REVIEWED | Posted: 12 January 2017 doi:10.20944/preprints201701.0063.v1

relaxations and electronic calculations are carried out using the density functional theory within the Perdew–Burke–Ernzerhof (PBE) generalized gradient approximation (GGA) [53], as implemented in the Vienna *ab initio* simulation package (VASP) [54]. The electron-ion interaction in the valence space is described by the projector augmented wave (PAW) method [55] with $2s^2 2p^1$ and $5p^6 5d^2 6s^2$ as the valence electrons for B and Hf, respectively. The plane-wave cutoff energy of 520 eV and a *k*-mesh of $2\pi \times 0.03$ Å^{-1} within the Monkhorst-Pack scheme [56] are selected to sample the Brillouin zone, which can make sure that all the total energy calculations are well converged to better than 1 meV/atom. The phonon calculation is achieved by using a supercell approach as implemented in the PHONOPY code [57,58]. The elastic constants C_{ij} are calculated by the strain-stress method, while the bulk modulus B and shear modulus G are derived from the Voigt–Reuss–Hill approximation [59]. Young's modulus E and Poisson's ratio v are obtained by the equations $E=9GB/(3B+G)$ and $v=(3B-2G)/(6B+2G)$ [59], respectively. The theoretical Vickers hardness is estimated by the hardness model proposed by Chen et al. [60].

3. Results and discussion

We have performed variable-cell structure prediction simulations using the evolutionary methodology for HfB_4 containing 1-4 f.u. in the simulation cell at 0 GPa. Our simulations predict a new orthorhombic structure with *Cmcm* symmetry, as shown in Figure 1. Within this *Cmcm* structure, it contains four HfB_4 f.u. in a unit cell. At 0 GPa, the optimized equilibrium lattice parameters and cell volume per f.u. are a_0=5.360 Å, b_0=3.134 Å, c_0=10.356 Å, and V_0=43.5 Å^3, in which two inequivalent Hf and B atoms occupy the Wyckoff 4*c* (0, 0.4189, 0.75) and 16*h* (0.8309, 0.8766, 0.5796) sites, respectively. Figure 1a is the polyhedral view for the *Cmcm* structure, and it shows an intriguing B–Hf–B sandwiches stacking order along the *c*-axis. In this structure, B atoms form parallel hexagonal planes, and each metal Hf atom is coordinated by 12 neighboring B atoms, forming HfB_{12} hexagonal columns which are connected by edges and boron hexagonal planes. For each HfB_{12} hexagonal column, the calculated Hf–B bond distances are 2.447(×4), 2.505 (×4), and 2.611 (×4) Å, and the B–B bond distances are calculated to be 1.791 (×8) and 1.822 (×4) Å. Note that the shortest B–B bond in our predicted *Cmcm* phase is smaller than that in the known hard materials ReB_2 (1.81 Å) [61],

Preprints (www.preprints.org) | NOT PEER-REVIEWED | Posted: 12 January 2017 doi:10.20944/preprints201701.0063.v1

OsB_2 (1.85 Å) [62], and HfB_2 (1.813 Å) [42]. For two neighbouring B layers, the calculated B-B bonding distances are 1.822 (×6) Å.

The thermodynamic stability of a compound can be described by the energy of its most stable phase. Thus we calculate the total energy per f.u. as a function of volume for six different phases of HfB_4. Here, the previously known five structures of YB_4 (No, 127, *P*4/*mbm*), ReP_4 (No, 61, *Pbca*), FeB_4 (No, 58, *Pnnm*), CrB_4 (No, 71, *Immm*), and MnB_4 (No, 14, $P2_1/c$) are also considered for HfB_4. This is because these compounds have been synthesized experimentally and are thermodynamically stable. Figure 2 reveals that the predicted *Cmcm*-HfB_4 phase has the smallest total energy in contrast to the other phases, indicating that it is indeed the ground state. For future experimental synthesis, we also calculate the formation enthalpies of the predicted *Cmcm* and considered structures for HfB_4 in the pressure range of 0-50 GPa. The formation enthalpy of HfB_4 with respect to the separate phases can be evaluated by the following equation $\Delta H = H_{HfB_4} - H_{Hf} - 4H_B$, where ΔH denotes the formation enthalpy, and the hexagonal Hf (space group $P6_3/mmc$) and α-B (space group *R*-3*m*) phases are selected as the reference structures. Figure 3 presents the dependence of the calculated formation enthalpy for HfB_4 on the pressure. Clearly, all the formation enthalpy-pressure curves show that the stabilities of HfB_4 with different structures gradually increase with increasing the pressure, reflecting that the high pressure is helpful to their stabilities. Notably, the predicted phase is the most stable phase of all the consider structures in the whole pressure range. The present calculations suggest that the *Cmcm*-HfB_4 phase can be synthesized at ambient conditions, thus further experimental synthesis is strongly desirable.

At 0 K, a stable crystal structure requires all phonon frequencies to be positive. Therefore, we have performed the calculations on the phonon dispersion curve for the predicted *Cmcm*-HfB_4 phase at 0 GPa and 50 GPa, respectively, and the corresponding results are given in Figure 4a and 4b. As shown in these two figures, the inexistence of any imaginary phonon frequency in the whole Brillouin zone supports its dynamical stability up to 50 GPa.

The mechanical stability is one necessary condition for the existence of a crystal. Accurate elastic constants can not only help us to understand the mechanical properties but also provide a useful information for estimating material hardness. By using a strain-stress method, we

Preprints (www.preprints.org) | NOT PEER-REVIEWED | Posted: 12 January 2017 doi:10.20944/preprints201701.0063.v1

obtain the elastic constants C_{ij} of the *Cmcm*-HfB_4 phase at 0 GPa. The calculated results are listed Table 1 along with the theoretical values and available experimental data of other hafnium borides [39,40,43-45,48], ZrB_{12} [63-65], TMB_4 (TM=Y [66], Fe [13,67,68], Cr [13,69], Mn [70], Zr [23], and Ta [27]). For a sable orthorhombic structure, the independent elastic stiffness tensor consist of nine components C_{11}, C_{22}, C_{33}, C_{44}, C_{55}, C_{66}, C_{12}, C_{13}, and C_{23}, and its mechanical stability criteria is given by [71,72], $C_{ii}>0$ (i=1, 2, 3, 4, 5, 6), $C_{11}+C_{22}+C_{33}+2(C_{12}+C_{13}+C_{23})>0$, $C_{11}+C_{22}-2C_{12}>0$, $C_{11}+C_{33}-2C_{13}>0$, and $C_{22}+C_{33}-2C_{23}>0$. From Table 1, the calculated elastic constants of the predicted *Cmcm*-HfB_4 phase satisfy completely the mechanical stability criteria, indicating that it is mechanically stable at ambient conditions. On the other hand, the positive eigenvalues of the elastic constant matrix for the predicted *Cmcm* phase further confirms that it is elastically stable. The values of C_{11}, C_{22}, and C_{33} for the compound are all higher than 500 GPa, suggesting that it is extremely difficult to be compressed along *a*-axis, *b*-axis, and *c*-axis, respectively. Moreover, the calculated C_{11} and C_{22} values are much larger than that of C_{33}, manifesting that the bond strengths along the [100] and [010] directions are much stronger than that the [001] direction. C_{44} is an important parameter indirectly governing the indentation hardness of a material. The studied *Cmcm* structure possesses a large C_{44} value of 251 GPa, meaning its relatively strong strength against the shear deformation.

From the obtained elastic constants, it is easy to calculate the bulk modulus B, shear modulus G, Young's modulus E, and Poisson's ratio v [59]. The calculated bulk modulus, shear modulus, Young's modulus, and Poisson's ratio of the *Cmcm* phase together with the reference materials mentioned above are tabulated in Table 2. As shown in Table 2, the calculated bulk modulus of the *Cmcm*-HfB_4 (243 GPa) is larger than those of HfB [39,40], ZrB_{12} [63-65], and YB_4 [8, 66] but is comparable to those of HfB_2 [43-45], HfB_{12} [48], and other TMB_4 (TM= Fe [12,13,67,68], Cr [13,14,69], Mn [11,70], Zr [23], and Ta [27]), indicating its strong ability to resist the volume deformation. Moreover, the bulk modulus (B=243 GPa) for the *Cmcm*-HfB_4 is in consistent with that directly obtained from the fitting results (B_0=244 GPa) of the third-order Birch-Murnaghan equation of states, which further demonstrates the good accuracy of our elastic calculations. To further compare the compressibility of the *Cmcm*-HfB_4 and other hafnium borides, the volume compression as a function of pressure is displayed in Figure 5, in

Preprints (www.preprints.org) | NOT PEER-REVIEWED | Posted: 12 January 2017 doi:10.20944/preprints201701.0063.v1

which the incompressibility curves of *c*-BN and diamond are also considered for comparison. As seen from this figure, all the considered hafnium borides except for HfB have almost the same incompressibility because of their very close bulk moduli, but they are more compressible than the *c*-BN and diamond. Compared with the bulk modulus, the shear modulus of a material describes its resistance to the shear deformation and is a more accurate predictor of the potential hardness. From Table 2, the calculated shear module for the predicted *Cmcm* phase is 240 GPa, which is bigger than those of HfB [39,40], HfB_{12} [48], ZrB_{12} [63,64], YB_4 [66], FeB_4 [13,67,68], MnB_4 [70], ZrB_4 [23], and TaB_4 [27] but very close to those of HfB_2 [43-46] and CrB_4 [13,69]. This suggests that the *Cmcm*-HfB_4 may be a potential superhard material. Besides the bulk and shear moduli, the Young's modulus can also provide a good measure of the stiffness of materials. Interestingly, the Young's modulus (542 GPa) of the *Cmcm*-HfB_4 except HfB_2 and MnB_4 exceeds those of the other considered compounds, therefore, the *Cmcm*-HfB_4 is a hard material. In addition, the ratio between the shear modulus and bulk modulus G/B can describe the brittleness or ductility of materials. According to Pugh criterion [73], if G/B is lower than 0.57, the material is ductile, otherwise the material behaves in a brittle way. As shown in Table 2, the ration G/B for the predicted *Cmcm* phase is 0.987, implying its brittle nature. The Poisson's ratio v is indicative of the degree of directionality for the covalent bonds. The typical v value is 0.1 for covalent materials and 0.33 for metallic materials [27]. From Table 2, the v value (0.128) of the *Cmcm*-HfB_4 is far below 0.33, and meanwhile the *Cmcm*-HfB_4 phase almost possesses the smallest v value among the considered borides, indicating that the *Cmcm*-HfB_4 has a strong covalent bond character. Debye temperature Θ_D is known as an important fundamental parameter of materials, and it is closely related to many physical properties like specific heat, elastic constants, and melting temperature [74]. At low temperature, the vibrational excitations arise only from the acoustic vibrations. Thus the Debye temperature can be derived from the elastic constants at low temperature [74-76]. At 0 GPa and 0 K, our calculated Debye temperature is 845 K for the *Cmcm*-HfB_4, which is lower than those of HfB_{12}, ZrB_{12} [63-65], YB_4 [66], and FeB_4 [67,68], but much larger than the values of the known ultra-incompressible material ReB_2 (755.5 K) [77], OsB_2 (601.09 K, 591 K) [78,79], RuB_2 (780 K) [79], ReN_2 (735 K) [80], and HfB_2 [44,46]. All these results suggest that the *Cmcm*-HfB_4 is a potential candidate as superhard

Preprints (www.preprints.org) | NOT PEER-REVIEWED | Posted: 12 January 2017 doi:10.20944/preprints201701.0063.v1

materials.

Through the above analysis, the predicted *Cmcm*-HfB_4 exhibits the high bulk modulus and large shear modulus as well as the high Debye temperature. Therefore, the hardness calculation is of great interest. The hardness of a material is the intrinsic resistance to deformation when a force is loaded, which depends upon the loading force and the sample quality. The Vickers hardness of a material is estimated by [60]

$$H_v = 2(K^2G)^{0.585} - 3, \quad (1)$$

where G is the shear modulus and $K = G/B$ is the Pugh modulus ratio. In view of this model, the calculated Vickers hardness for the predicted *Cmcm*-HfB_4 is 45.7 GPa, which exceeds 40 GPa and is comparable to the known superhard materials *c*-BN (48 GPa) [81], γ-B_{28} (50 GPa) [82], and B_6O (45 GPa) [3]. Accordingly, it is conceivable that the *Cmcm*-HfB_4 may be a superhard material.

The elastic anisotropy of a crystal is important to further investigate the physical and chemical characteristics. For superhard materials, it should preferably be isotropic, otherwise it will deform at a given direction. Therefore, it is extremely necessary to study the elastic anisotropy in order to improve their mechanical durability. The shear anisotropic factors offer a measure of the degrees of anisotropy in atomic bonding in different planes. The shear anisotropic factor [72,74] for the {100} shear planes between the <011> and <010> directions is

$$A_1 = \frac{4C_{44}}{C_{11} + C_{33} - 2C_{13}}. \quad (2)$$

For the {010} shear planes between the <101> and <001> directions, it is defined as

$$A_2 = \frac{4C_{55}}{C_{22} + C_{33} - 2C_{23}}. \quad (3)$$

The shear anisotropic factor for the {001} shear planes between the <110> and <010> directions is expressed by

Preprints (www.preprints.org) | NOT PEER-REVIEWED | Posted: 12 January 2017 doi:10.20944/preprints201701.0063.v1

$$A_3 = \frac{4C_{66}}{C_{11} + C_{22} - 2C_{12}}. \quad (4)$$

For an isotropic crystal, the factors A_1, A_2, and A_3 must be 1.0, while any departure from 1.0 is a measure of the degree of elastic anisotropy possessed by the crystal. The calculated shear anisotropic factors for A_1, A_2, and A_3 are 1.062, 0.858, and 0.950 but not 1.0, respectively, indicating that the *Cmcm*-HfB_4 has a certain degree of the elastic anisotropy. These results also show that the elastic anisotropy for the {100} shear planes between the <011> and <010> directions is nearly the same as that for the {001} shear planes between the <110> and <010> directions, but smaller than that for the {010} shear planes between the <101> and <001> directions. In addition, the shear anisotropic factor A_2 for the {010} shear planes between the <101> and <001> directions is more departure from 1.0 compared with other two factors, hence, the {010} shear planes are easier to be the cleavage planes among these principal planes. For the orthorhombic crystal, the shear anisotropic factors are insufficient to describe the elastic anisotropy. Therefore, we also investigate the elastic anisotropy which comes from the anisotropy of the linear bulk modulus. The directional bulk modulus along different crystal axes can be defined as $B_i = idP/di$ (i = a, b, c) [67,74]. The calculated B_a, B_b, and B_c are 751 GPa, (784 GPa), and 662 GPa, repectively. This indicates that the compressibility along the *a* and *b* axis is lower than those along the *c* axes, which is in agreement with our predicted elastic constants values of C_{11}, C_{22}, and C_{33}.

To visually illustrate the elastic anisotropy, we investigate the directional dependences of the Young's modulus, bulk modulus, and shear modulus, respectively. For the orthorhombic *Cmcm*-HfB_4, the Young's modulus E and bulk modulus B are given by [68,74]

$$E^{-1} = s_{11}\alpha^4 + s_{22}\beta^4 + s_{33}\gamma^4 + 2s_{12}\alpha^2\beta^2 + 2s_{13}\alpha^2\gamma^2 + 2s_{23}\beta^2\gamma^2 + s_{66}\alpha^2\beta^2 + s_{55}\alpha^2\gamma^2 + s_{44}\beta^2\gamma^2, \quad (5)$$

$$B^{-1} = (s_{11} + s_{12} + s_{13})\alpha^2 + (s_{12} + s_{22} + s_{23})\beta^2 + (s_{13} + s_{23} + s_{33})\gamma_2, \quad (6)$$

where α, β, and γ are the direction cosines of [*uvw*] direction and s_{ij} are the elastic compliance constants which are obtained by Nye [83]. The shear modulus G on the (*hkl*) shear plane with the shear stress applied alone the [*uvw*] direction is written as [68,74]

Preprints (www.preprints.org) | NOT PEER-REVIEWED | Posted: 12 January 2017 doi:10.20944/preprints201701.0063.v1

$$G^{-1} = 4(s_{11}\alpha_1^2\alpha_2^2 + s_{22}\beta_1^2\beta_2^2 + s_{33}\gamma_1^2\gamma_2^2) + 8(s_{12}\alpha_1\alpha_2\beta_1\beta_2 + s_{13}\alpha_1\alpha_2\gamma_1\gamma_2 + s_{23}\beta_1\beta_2\gamma_1\gamma_2) + s_{44}(\beta_1\gamma_2 + \beta_2\gamma_1)^2 + s_{55}(\alpha_1\gamma_2 + \alpha_2\gamma_1)^2 + s_{66}(\alpha_1\beta_2 + \alpha_2\beta_1)^2 \quad (7)$$

where α_1, β_1, γ_1, α_2, β_2, γ_2 are the direction cosines of the [*uvw*] and [*HKL*] directions in the coordinate systems, and the [*HKL*] direction shows the vector normal to the (*hkl*) shear plane.

The three-dimensional surface representations which show the variation of the Young's modulus and bulk modulus of the *Cmcm*-HfB_4 are illustrated in Figure 6a and 6c, respectively. For a perfectly isotropic crystal, it will be a spherical shape, while any deviation from a spherical shape can directly indicate the degree of the elastic anisotropy in the crystal. From Figure 6a and 6c, the Young's modulus presents a well-pronounced anisotropy due to the evidently nonspherical nature, whereas the bulk modulus nearly exhibits an isotropy because of a small deviation from a spherical shape. Moreover, the projections of the Young's modulus and bulk modulus on the *ab*, *ac*, and *bc* planes are plotted in Figure 6b and 6d. Though in-plane anisotropy is almost nonexistent in the *ab* plane, in-plane anisotropies in the *ac* and *bc* planes are obviously revealed. To well understand the variation of the Young's modulus alone different directions, we study the directional dependences of the Young's modulus alone tensile axis in the (100), (010), (001), and $(1\bar{1}0)$ planes, respectively, and the calculated results are shown in Figure 7a. For the orientation dependences of the Young's modulus from [001] to [010] in the (100) plane, the *Cmcm*-HfB_4 has a maximum of $E_{[010]} = 589.3$ GPa and a minimum of $E_{[001]} = 479.8$ GPa. For the (010) plane, the Young's modulus alone the [001] direction exhibits the minimal value ($E_{[001]} = 479.8$ GPa) and the Young's modulus alone the [100] direction possesses the maximal one ($E_{[100]} = 590.1$ GPa). For the (001) plane, the Young's modulus does not depend on the tensile stress direction, which is in good consistent with the result presented in Figure 6b. For the change of the Young's modulus in the $(1\bar{1}0)$ plane for the quadrant of directions between [001] and [110], the maximum and minimum values of the Young's modulus are $E_{[110]} = 619.7$ GPa and $E_{[001]} = 479.8$ GPa, respectively. Consequently, the order of the Young's modulus as a function of the principal crystal tensile [*uvw*] for the *Cmcm*-HfB_4 is summarized as below, $E_{[110]} > E_{[100]} > E_{[010]} > E_{[001]}$. In order to

Preprints (www.preprints.org) | NOT PEER-REVIEWED | Posted: 12 January 2017 doi:10.20944/preprints201701.0063.v1

understand the plastic deformation for the *Cmcm*-HfB_4, the dependence of the shear modulus on the stress direction is also investigated, and the calcuated result is shown in Figure 7b. For the (100) shear plane, we let θ be the angle between the shear stress direction and [001]. In this case, $\alpha_1 = 0$, $\beta_1 = \sin\theta$, $\gamma_1 = \cos\theta$, $\alpha_2 = 1$, $\beta_2 = \gamma_2 = 0$, and $G^{-1} = (s_{55} - s_{66})\cos^2\theta + s_{66}$. Because $s_{55} > s_{66}$, the shear modulus is the largest along the [010] direction ($G_{max} = 264$ GPa) and the smallest along the [001] direction ($G_{min} = 197$ GPa). For the (010) shear plane with the shear stress direction rotated from [001] to [100], the direction cosines are $\alpha_1 = \sin\theta$, $\beta_1 = 0$, $\gamma_1 = \cos\theta$, $\alpha_2 = \gamma_2 = 0$, and $\beta_2 = 1$, where θ is the angle between the shear stress direction and [001], so one can obtain $G^{-1} = (s_{44} - s_{66})\cos^2\theta + s_{66}$ from Eq. (7). In our calculations, due to $s_{44} \approx s_{66}$, the shear modulus is simplified into $G^{-1} = s_{66}$, thus the shear modulus is nearly independent of the shear stress direction, as shown by the magenta curve in Figure 7b. For the (001) shear plane with the shear stress direction varied from [100] to [010], θ is the angle between the shear stress direction and [100], and the direction cosines are $\alpha_1 = \cos\theta$, $\beta_1 = \sin\theta$, $\gamma_1 = 0$, $\alpha_2 = \beta_2 = 0$, and $\gamma_2 = 1$, so the shear module can be written as $G^{-1} = s_{44} + (s_{55} - s_{44})\cos^2\theta$. Since $s_{55} > s_{44}$, the maximal value of the shear modulus is 251 GPa for the [010] direction and the minimal one of the shear modulus is 197 GPa for the [100] direction. When the $(1\bar{1}0)$ plane is the shear plane and the shear stress direction is changed from [001] to [110], the shear modulus is the highest when $\theta = 90^\circ$ and the lowest when $\theta = 0^\circ$, which corresponds to $G_{max} = 274.2$ GPa for the [110] direction and $G_{min} = 234.6$ GPa for the [001] direction.

The electronic structure is the key for the understanding of the mechanical properties of the *Cmcm*-HfB_4, the total and partial densities of states (DOS) are calculated and plotted in Figure 8, where the vertical dashed line denotes the Fermi level. Clearly, the *Cmcm*-HfB_4 presents a metallic character because of the finite value of the DOS at the Fermi level, which mainly originates from the B-2*p* and Hf-5*d* electrons. As seen from partial DOS profiles, the

Preprints (www.preprints.org) | NOT PEER-REVIEWED | Posted: 12 January 2017 doi:10.20944/preprints201701.0063.v1

peaks below -8.4 eV are mainly contributed by B-2*s* and B-2*p* states with slight contributions from the 5*p*, 5*d*, and 6*s* electrons of Hf. The states above -8.4 eV primarily arises from Hf-5*d* and B-2*p* orbitals with small contributions of B-2*s*, Hf-5*p* and Hf-6*s*. Furthermore, the partial DOS profiles for the Hf-5*d* and B-2*p* have very similar shapes in the energy range from -8.4 eV to the Fermi level, which indicates the strong hybridization between the Hf-5*d* and B-2*p* orbitals. This fact also reveals the existence of a strong covalent interaction between the Hf and B atoms. For the total DOS, the typical feature is the presence of so-called pseudogap, which is deemed as the borderline between the bonding states and antibonding states [84,85]. Note that the Fermi energy is perfectly lying on the pseudogap for the *Cmcm*-HfB_4 phase. This implies that the *s*-*p* and *p*-*d* bonding states begin to be saturated. Both the full occupation of the bonding states and without filling on the antibonding states results in the high bulk modulus and large shear modulus, small Poisson's ratio, and also enhances the structural stability of HfB_4.

A deeper insight of the chemical bonding property of the *Cmcm*-HfB_4 can be obtained by calculating the electronic localization function (ELF). The ELF is a contour plot in real space and its value is scaled between 0 and 1. ELF=1 shows the perfect localization property of covalent bonds or lone pair (filled core levels), ELF=0 is typical for a vacuum (no electron density) or regions between atomic orbitals, and ELF = 0.5 corresponds to the perfect free-electron gas, with values of this order meaning regions with bonding of a metallic character. It should be noted that the ELF is usually used to distinguishing metallic, covalent, and ionic bonding. The calculated ELF contours of the predicted *Cmcm*-HfB_4 phase on the (001) and $(\bar{1}01)$ planes are plotted in Figure 9. According to the definition of the ELF, we can deduce that there is the existence of strong covalent B-B bonding within the planar six-membered ring unit due to the large ELF value between two adjacent B and B atoms. Moreover, one can see clearly from Figure 9b that the high ELF value between the Hf and B atoms indicates the partially B-Hf covalent bonding interaction in the *Cmcm*-HfB_4 phase, although not as strong as B-B bonding. Therefore, the strong covalent interaction between the B-B and B-Hf bonds is the major driving force for its high hardness.

4. Conclusions

Preprints (www.preprints.org) | NOT PEER-REVIEWED | Posted: 12 January 2017 doi:10.20944/preprints201701.0063.v1

In conclusion, a new orthorhombic *Cmcm* structure is predicted to be the ground state for HfB_4 by combining the PSO algorithm with first-principles calculations, and it is energetically more favorable than the earlier proposed YB_4-, ReP_4-, FeB_4-, CrB_4-, and MnB_4-type structures in the pressure range of 0-50 GPa. The calculated phonon dispersion, formation enthalpy, elastic constants have demonstrated that the *Cmcm* phase is dynamically stable, experimentally synthesizable, and mechanically stable under ambient conditions. The predicted high bulk modulus, large shear modulus, and small Poisson's ratio have indicated that the *Cmcm*-HfB_4 is a low-compressible material. Based on the estimated Vickers hardness (45.7 GPa) for the *Cmcm*-HfB_4, it is a potential superhard material. In addition, the directional dependences of the Young's modulus, bulk modulus, and shear modulus for HfB_4 are also investigated for characterizing the elastic property and anisotropy. The electronic densities of states and ELF analyses have further confirmed that the strong covalent B-B and B-Hf bonds play a key role in the incompressibility and hardness of HfB_4. We hope that our theoretical findings will inevitably stimulate further experimental works on this material in the future.

Acknowledgements: The authors acknowledge the Science Foundation of Baoji University of Arts and Sciences of China (Grant Nos. ZK16069 and ZK11135), the Natural Science Foundation of the Education Committee of Shaanxi Province, China (Grant No. 2013JK0637), the Natural Science Basic Research Plan in Shaanxi Province of China (Grant Nos. 2016JM1012 and 2014JM8347), and the Natural Science Foundation of China (Grant Nos. 11404008 and 11647007).

Author Contributions: Gangtai Zhang and Yanfei Hu designed the project; Rui Gao and Tingting Bai performed the calculations; Gangtai Zhang, Rui Gao, and Yaru Zhao wrote the manuscript; Yanfei Hu revised the paper and coordinated the work; all authors discussed results.

Conflicts of Interest: The authors declare no conflict of interest.

References

1. Occelli, F.; Farber, D. L.; Toullec, R. L. Properties of diamond under hydrostatic pressures up to 140 GPa. *Nat. Mater.* **2003**, *2*, 151-154.
2. Zhang, Y.; Sun, H.; Chen, C.F. Structural deformation, strength and instability of cubic

 doi:10.20944/preprints201701.0063.v1

BN compared to diamond: a first-principles study. *Phys. Rev. B* **2006**, *73*, 144115.

3. He, D.W.; Zhao, Y.S.; Daemen, L.; Qian, J.; Shen, T.D.; Zerda, T.W. Boron suboxide: as hard as cubic boron nitride. *Appl. Phys. Lett.* **2002**, *81*, 643–645.
4. Solozhenko, V.L.; Andrault, D.; Fiquet, G.; Mezouar, M.; Rubie, D.C. Synthesis of superhard cubic BC_2N. *Appl. Phys. Lett.* **2001**, *78*, 1385-1387.
5. Chung, H.Y.; Weinberger, M.B.; Levine, J.B.; Kavner, A.; Yang, J.M.; Tolbert, S.H.; Kaner, R.B. Synthesis of ultra-incompressible superhard rhenium diboride at ambient pressure. *Science* **2007**, *316*, 436–439.
6. Cumberland, R.W.; Weinberger, M.B.; Gilman, J.J.; Clark, S.M.; Tolbert, S.H.; Kaner, R.B. Osmium diboride, an ultra-incompressible, hard material. *J. Am. Chem. Soc.* **2005**, *127*, 7264–7265.
7. Chung, H.Y.; Weinberger, M.B.; Yang, J.M.; Tolbert, S.H.; Kaner, R.B. Correlation between hardness and elastic moduli of the ultraincompressible transition metal diborides RuB_2, OsB_2, and ReB_2. *Appl. Phys. Lett.* **2008**, *92*, 261904.
8. Waśkowska, A.; Gerward, L.; Olsen, J.S.; Babu, K.R.; Vaitheeswaran, G.; Kanchana, V.; Svane, A.; Filipov, V.B.; Levchenko, G.; Lyaschenko, A. Thermoelastic properties of ScB_2, TiB_2, YB_4 and HoB_4: experimental and theoretical studies. *Acta Mater.* **2011**, *59*, 4886-4894.
9. Litterscheid, C.; Knappschneider, A.; Albert, B. Single crystal structure of MnB_4. *Z. Anorg. Allg. Chem.* **2012**, *638*, 1608.
10. Knappschneider, A.; Litterscheid, C.; George, N.C.; Brgoch, J.; Wagner, N.; Beck, J.; Kurzman, J.A.; Seshadri, R.; Albert, B. Peierls-distorted monoclinic MnB_4 with a Mn-Mn bond. *Angew. Chem. Int. Ed*. **2014**, *53*, 1684-1688.
11. Gou, H.Y.; Tsirlin, A.A.; Bykova, E.; Abakumov, A.M.; Tendeloo, G.V.; Richter, A.; Ovsyannikov, S.V.; Kurnosov, A.V.; Trots, D.M.; Konôpková, Z.; Liermann, H.P.; Dubrovinsky, L.; Dubrovinskaia, N. Peierls distortion, magnetism, and high hardness of manganese tetraboride. *Phys. Rev. B* **2014**, *89*, 064108.
12. Gou, H.Y.; Dubrovinskaia, N.; Bykova, E.; Tsirlin, A.A.; Kasinathan, D.; Schnelle, W.; Richter, A.; Merlini, M.; Hanfland, M.; Abakumov, A.M.; Batuk, D.; Tendeloo, G.V.; Nakajima, Y.; Kolmogorov, A.N.; Dubrovinsky, L. Discovery of a superhard iron

tetraboride superconductor. *Phys. Rev. Lett.* **2013**, *111*, 157002.

13. Niu, H.Y.; Wang, J.Q.; Chen, X.Q.; Li, D.Z.; Li, Y.Y.; Lazar, P.; Podloucky, R.; Kolmogorov, A.N. Structure, bonding, and possible superhardness of CrB_4. *Phys. Rev. B* **2012**, *85*, 144116.
14. Wang, S.; Yu, X.; Zhang, J.; Zhang, Y.; Wang, L.; Leinenweber, K.; Xu, H.; Popov, D.; Park, C.; Yang, W.; He, D.; Zhao, Y. Crystal structures, elastic properties, and hardness of high-pressure synthesized CrB_2 and CrB_4. *J. Superhard Mater.* **2014**, *36*, 279-287.
15. Gu, Q.F.; Krauss, G.; Steurer, W. Transition metal borides: superhard versus ultra-incompressible. *Adv. Mater.* **2008**, *20*, 3620–3626.
16. Liang, Y.C.; Yuan, X.; Zhang, W.Q. Thermodynamic identification of tungsten borides. *Phys. Rev. B* **2011**, *83*, 220102(R).
17. Zhang, R.F.; Legut, D.; Lin, Z.J.; Zhao, Y.S.; Mao, H.K.; Veprek, S. Stability and strength of transition-metal tetraborides and triborides. *Phys. Rev. Lett.* **2012**, *108*, 255502.
18. Gou, H.Y.; Li, Z.P.; Wang, L.M.; Lian, J.; Wang, Y.C. Peculiar structure and tensile strength of WB_4: nonstoichiometric origin. *AIP Adv.* **2012**, *2*, 012171.
19. Liang, Y.C.; Fu, Z.; Yuan, X.; Wang, S.M.; Zhong, Z.; Zhang, W.Q. An unexpected softening from WB_3 to WB_4. *Europhys. Lett.* **2012**, *98*, 66004.
20. Li, P.F.; Zhou, R.L.; Zeng, X.C. Computational analysis of stable hard structures in the Ti-B system. *ACS Appl. Mater. Inter.* **2015**, *7*, 15607-15617.
21. Wu, L.L.; Wan, B.; Zhao, Y.; Zhang, Y.K.; Liu, H.Y.; Wang, Y.C.; Zhang, J.W.; Gou, H.Y. Unraveling stable vanadium tetraboride and triboride by first-principles computations. *J. Phys. Chem. C* **2015**, *119*, 21649-21657.
22. Niu, H.Y.; Chen, X.Q.; Ren, W.J.; Zhu, Q.; Oganov, A.R.; Li, D.Z.; Li, Y.Y. Variable-composition structural optimization and experimental verification of MnB_3 and MnB_4. *Phys. Chem. Chem. Phys.*, **2014**, *16*, 15866-15873.
23. Zhang, X.Y.; Qin, J.Q.; Sun, X.W.; Xue, Y.A.; Ma, M.Z.; Liu, R.P. First-principles structural design of superhard material of ZrB_4. *Phys. Chem. Chem. Phys.* **2013**, *15*, 20894-20899.
24. Li, X.F.; Han, L.G.; Hou, Y.S.; Yan, H.Y.; Hu, Z.Y.; Zhang, S.L. New ultra-incompressible phases of NbB_4 predicted from first principles. *Phys. Lett. A* **2017**,

 doi:10.20944/preprints201701.0063.v1

381, 362-367.

25. Zhang, M.G.; Wang, H.; Wang, H.B.; Cui, T.; Ma, Y.M. Structural modifications and mechanical properties of molybdenum borides from first principles. *J. Phys. Chem. C* **2010**, *114*, 6722-6725.
26. Zhang, M.G.; Yan, H.Y.; Wei, Q.; H. Wang, Universal ground state hexagonal phases and mechanical properties of stoichiometric transition metal tetraborides: TMB_4(TM = W, Tc, and Re). *Comput. Mater. Sci.*, **2013**, *68*, 371-378.
27. Chu, B.H.; Li, D.; Bao, K.; Tian, F.B.; Duan, D.F.; Sha, X.J.; Hou, P.G.; Liu, Y.X.; Zhang, H.D.; Liu, B.B.; Cui, T. Ultrahard boron-rich tantalum boride: monoclinic TaB_4. *J. Alloy. Compd.* **2014**, *617*, 660-664.
28. Wang, B.; Wang, D.Y.; Wang, Y.X. A new hard phase of ReB_4 predicted from first principles. *J. Alloy. Compd.* **2013**, *573*, 20-26.
29. Zhang, M.G.; Yan, H.Y.; Zhang, G.T.; Wang, H. Ultra-incompressible orthorhombic phase of osmium tetraboride (OsB_4) predicted from first principles. *J. Phys. Chem. C* **2012**, *116*, 4293-4297.
30. Li, X.F.; Wang, H.Y.; Lv, J.; Liu, Z.L. Phase diagram and physical properties of iridium tetraboride from first-principles. *Phys. Chem. Chem. Phys.* **2016**, *18*, 12569-12575.
31. Rogl, P.; Potter, P.E. A critical review and thermodynamic calculation of the binary system: hafnium-boron. *Calphad* **1988**, *12*, 207-218.
32. Rudy, E.; Benesovsky, F. Untersuchungen in den systemen: hafnium-bor-stickstof und zirconium-bor-stickstoff. *Monatsh. Chem.* **1961**, *92*, 415-441.
33. Kaufman, L.; Clougherty, E.V. Investigation of boride compounds for very high temperature applications. *ManLabs, Inc., Cambridge, MA, Air Force Technical Documentary Report No. RTD-TDR-63-4096*, **1963**.
34. Goncharov, A.A.; Dub, S.N.; Agulov A.V. Structure, composition, and physicomechanical characteristics of HfB_2 and Hf-BN films. *Phys. Metals Metallogr.* **2013**, *114*, 95-101.
35. Cannon, J.F.; Farnsworth, P.B. High pressure syntheses of ThB_{12} and HfB_{12}. *J. Less-Common Met*. **1983**, *92*, 359-368.
36. Portnoi, K.I.; Romashov, V.M.; Romanovich, I.V.; Levinskii, Y.V.; Prokof'sev, S.A. Phase diagram of the hafnium-boron system. *Inorg. Mater.* **1972**, *7*, 1769-1772.

37. Akopov, G.; Yeung, M.T.; Turner, C.L.; Li, R.L.; Kaner, R.B. Stabilization of HfB_{12} in $Y_{1-x}Hf_xB_{12}$ under ambient pressure. *Inorg. Chem*. **2016**, *55*, 5051−5055.
38. Xu, X.W.; Fu, K.; Li, L.L.; Lu, Z.M.; Zhang, X.H.; Fan, Y.; Lin, J.; Liu, G.D.; Luo, H.Z.; Tang, C.C. Dependence of the elastic properties of the early-transition-metal monoborides on their electronic structures: a density functional theory study. *Physica B*, **2013**, *419*, 105–111.
39. Wang, Y.; Chen, W.; Chen, X.; Liu, H.Y.; Ding, Z.H.; Ma, Y.M.; Wang, X.D.; Cao, Q.P.; Jiang, J.Z. Crystal structures, stability, electronic and elastic properties of 4d and 5d transition metal monoborides: first-principles calculations. *J. Alloy. Compds*. **2012**, *538*, 115–124.
40. Huang, B.; Duan, Y.H.; Hu, W.C.; Sun, Y.; Chen, S. Structural, anisotropic elastic and thermal properties of MB (M=Ti, Zr and Hf) monoborides. *Ceram. Int.* **2015**, *41*, 6831–6843.
41. Opeka, M.M.; Talmy, I.G.; Wuchina, E.J.; Zaykoski, J.A.; Causey, S.J. Mechanical, thermal, and oxidation properties of refractory hafnium and zirconium compounds. *J. Eur. Ceram. Soc*. **1999**, *19*, 2405–2414.
42. Fahrenholtz, W.G.; Hilmas, G.E. Refractory diborides of zirconium and hafnium. *J. Am. Ceram. Soc*. **2007**, *90*, 1347–1364.
43. Shein, I.R.; Ivanovskii, A.L. Elastic properties of mono- and polycrystalline hexagonal AlB_2-like diborides of s, p and d metals from first-principles calculations. *J. Phys: Condens. Mat.* **2008**, *20*, 415218.
44. Zhang, X.H.; Luo, X.G.; Han, J.C.; Li, J.P.; Han, W.B. Electronic structure, elasticity and hardness of diborides of zirconium and hafnium: first principles calculations. *Comp. Mater. Sci.* **2008**, *44*, 411–421.
45. Lawson, J.W.; Bauschlicher, C.W.; Daw, M.S. Ab initio computations of electronic, mechanical, and thermal properties of ZrB_2 and HfB_2. *J. Am. Ceram. Soc.* **2011**, *94*, 3494–3499.
46. Wiley, D.E.; Manning, W.R.; Hunter, J.O. Elastic properties of polycrystalline TiB_2, ZrB_2 and HfB_2 from room temperature to 1300 °K. *J. Less-Common Met*. **1969**, *18*, 149-157.

 doi:10.20944/preprints201701.0063.v1

47. Bsenko, L.; Lundström, T. The high-temperature hardness of ZrB_2 and HfB_2. *J. Less-Common* Met. **1974**, *34*, 273-278.
48. Korozlu, N.; Colakoglu, K.; Deligoz, E.; Aydin, S. The elastic and mechanical properties of MB_{12} (M = Zr, Hf, Y, Lu) as a function of pressure. *J. Alloy Compds*. **2013**, *546*, 157–164.
49. Wang, Y.C.; Lv, J.; Zhu, L.; Ma, Y.M. Crystal structure prediction via particle-swarm optimization. *Phys. Rev. B* **2010**, *82*, 094116.
50. Wang, Y.C.; Lv, J.; Zhu, L.; Ma, Y.M. CALYPSO: a method for crystal structure prediction. *Comput. Phys. Commun*. **2012**, *183*, 2063−2070.
51. Wang, H.; Wang, Y.C.; Lv, J.; Li, Q.; Zhang, L.J.; Ma, Y.M. CALYPSO structure prediction method and its wide application. *Comput. Mater. Sci*. **2016**, *112*, 406−415.
52. Ma, Y.M.; Wang, Y.C.; Lv, J.; Zhu, L. http://www.calypso.cn.
53. Perdew, J.P.; Burke, K.; Ernzerhof, M. Generalized gradient approximation made simple. *Phys. Rev. Lett*. **1996**, *77*, 3865−3868.
54. Kresse, G.; Furthmüller, J. Efficient iterative schemes for *ab initio* total-energy calculations using a plane-wave basis set. *Phys. Rev. B* **1996**, *54*, 11169−11186.
55. Kresse, G.; Joubert, D. From ultrasoft pseudopotentials to the projector augmented-wave method. *Phys. Rev. B* **1999**, *59*, 1758−1775.
56. Monkhorst, H.J.; Pack, J.D. Special points for brillouin-zone integrations. *Phys. Rev. B* **1976**, *13*, 5188−5192.
57. Togo, A.; Oba, F.; Tanaka, I. First-principles calculations of the ferroelastic transition between rutile-type and $CaCl_2$-type SiO_2 at high pressures. *Phys. Rev. B* **2008**, *78*, 134106.
58. Togo, A.; Tanaka, I. First principles phonon calculations in materials science. *Scr. Mater.* **2015**, *108*, 1−5.
59. Hill, R. The elastic behaviour of a crystalline aggregate. *Phys. Soc. Lond. Sect. A* **1952**, *65*, 349−354.
60. Chen, X.Q.; Niu, H.; Li, D.; Li, Y. Modeling hardness of polycrystalline materials and bulk metallic glasses. *Intermetallics* **2011**, *19*, 1275−1281.
61. Wang, Y.X. Elastic and electronic properties of TcB_2 and superhard ReB_2: first-principles calculations. *Appl. Phys. Lett.* **2007**, *91*, 101904.

62. Šimůnek, A. Anisotropy of hardness from first principles: the cases of ReB_2 and OsB_2. *Phys. Rev. B* **2009**, *80*, 060103(R).
63. Ai, B.C.; Luo, X.G.; Yu, J.J.; Miao, W.B.; Hu, P. Theoretical elastic stiffness and thermodynamic properties of zirconium dodecaboride from first principles calculation. *Comput. Mater. Sci.* 2014, **82**, 37-44.
64. Chen, Z.Q.; Peng, Y.S.; Hu, M.; Li, C.M.; Luo, Y.T. Elasticity, hardness, and thermal properties of ZrB_n (n=1, 2,12). *Ceram Int.* **2016**, *42*, 6624–6631.
65. Grechnev, G.E.; Baranovskiy, A.E.; Fil, V.D.; Ignatova, T.V.; Kolobov, I.G.; Logosha, A.V.; Shitsevalova, N.Y.; Filippov, V.B.; Eriksson, O. Electronic structure and bulk properties of MB_6 and MB_{12} borides. *Low Temp. Phys*. **2008**, *34*, 921.
66. Fu, Y.Y.; Li, Y.W.; Huang, H.M. Elastic and dynamical properties of YB_4: first-principles study. *Chin. Phys. Lett.* **2014**, *31*, 116201.
67. Zhang, X.Y.; Qin, J.Q.; Ning, J.L.; Sun, X.W.; Li, X.T.; Ma, M.Z.; Liu, R.P. First principle study of elastic and thermodynamic properties of FeB_4 under high pressure. *J. Appl. Phys*. **2013**, *114*, 183517.
68. Zhang, M.G.; Yan, H.Y. Elastic anisotropy and thermodynamic properties of iron tetraboride under high pressure and high temperature. *Solid State Commun*. **2014**, *187*, 53–58.
69. Xu, H.B.; Wang, Y.X.; Lo, V.C. First-principles study of CrB_4 as a high shear modulus compound. *Phys. Status Solidi RRL* **2011**, *5*, 13–15.
70. Yang, M.; Wang, Y.C.; Yao, J.L.; Li, Z.P.; Zhang, J.; Wu, L.L.; Li, H.; Zhang, J.W.; Gou, H.Y. Structural distortion and band gap opening of hard MnB_4 in comparison with CrB_4 and FeB_4. *J. Solid State Chem.* **2014**, *213*, 52-56.
71. Wu, Z.J.; Zhao, E.J.; Xiang, H.P.; Hao, X.F.; Liu, X.J.; Meng, J. Crystal structures and elastic properties of superhard IrN_2 and IrN_3 from first principles. *Phys. Rev. B* **2007**, *76*, 054115.
72. Wei, Q.; Zhang, Q.; Zhang, M.G. Crystal structures and mechanical properties of Ca_2C at high pressure. *Materials* **2016**, *9*, 570.
73. Pugh, S.F. Relations between the elastic moduli and the plastic properties of polycrystalline pure metals. *Philos. Mag*. **1954**, *45*, 823-843.

74. Ravindran, P.; Fast, L.; Korzhavyi, P.A.; Johansson, B.; Wills, J.; Eriksson, O. Density functional theory for calculation of elastic properties of orthorhombic crystals: application to $TiSi_2$. *J. Appl. Phys*. **1998**, *84*, 4891-4904.
75. Anderson, O.L. A simplified method for calculating the Debye temperature from elastic constants. *J. Phys. Chem. Solids* **1963**, *24*, 909-917.
76. Zhang, G.T.; Bai, T.T.; Zhao, Y.R.; Hu, Y.F. A new superhard phase and physical properties of ZrB_3 from first-principles calculations. *Materials* **2016**, *9*, 703.
77. Aydin, S.; Simsek, M. First-principles calculations of MnB_2, TcB_2, and ReB_2 within the ReB_2-type structure. *Phys. Rev. B* **2009**, *80*, 134107.
78. Yang, J.W.; Chen, X.R.; Luo, F.; Ji, G.F. First-principles calculations for elastic properties of OsB2 under pressure. *Physica B* **2009**, *404*, 3608-3613.
79. Hao, X.F.; Xu, Y.H.; Wu, Z.J.; Zhou, D.F.; Liu, X.J.; Meng, J. Elastic anisotropy of OsB_2 and RuB_2 from first-principles study. *J. Alloys Compd*. **2008**, *453*, 413-417.
80. Li, Y.L.; Zeng, New potential super-incompressible phase of ReN_2. Z. *Chem. Phys. Lett*., **2009**, *474*, 93-96.
81. Sung, C.M.; Sung, M. Carbon nitride and other speculative superhard materials. *Mater. Chem. Phys*. 1996, **43**, 1-18.
82. Solozhenko, V.L.; Kurakevych, O.O.; Oganov, A.R. On the hardness of a new boron phase, orthorhombic γ-B_{28}. *J. Superhard Mater*. **2008**, *30*, 428-429.
83. Nye, J.F. Physical properties of crystals: their representation by tensors and matrices, Oxford University Press: New York, 1985.
84. Xu, J.H.; Freeman, A.J. Phase stability and electronic structure of $ScAl_3$ and $ZrAl_3$ and of Sc-stabilized cubic $ZrA1_3$ precipitates. *Phys. Rev. B* **1990**, *41*, 12553–12561.
85. Vajeeston, P.; Ravindran, P.; Ravi, C.; Asokamani, R. Electronic structure, bonding, and ground-state properties of AlB_2-type transition-metal diborides. *Phys. Rev. B* **2001**, *63*, 045115.

Preprints (www.preprints.org) | NOT PEER-REVIEWED | Posted: 12 January 2017 doi:10.20944/preprints201701.0063.v1

Table 1. The calculated elastic constants C_{ij} (GPa) for HfB_4.

structure	work	C_{11}	C_{22}	C_{33}	C_{44}	C_{55}	C_{66}	C_{12}	C_{13}	C_{23}
Cmcm-HfB_4	this work	606	611	505	251	197	264	53	83	99
Fm-3*m*-HfB	this work	403			69			58		
	theor. [39]	467			34			145		
	theor. [40]	413			56.2			63.1		
Pnma-HfB	this work	392	468	338	181	161	198	93	115	91
	theor. [40]	442.8	502.4	387.5	191.9	170.4	218.4	124.7	131.7	121.7
*P*6/*mmm*-HfB_2	this work	603		453	264		270	62	125	
	theor. [43]	592.7		481.3	262.3			99.6	141.3	
	theor. [44]	606		455	265			98	135	
	theor. [45]	609		470	266			73	135	
Fm-3*m*-HfB_{12}	this work	404			244			152		
	theor. [48]	436.4			250.8			156.1		
Fm-3*m*-ZrB_{12}	theor. [63]	412.6			244.4			141.3		
	theor. [64]	420			249			123		
	expt. [65]	443			265			129		
*P*4/*mbm*-YB_4	theor. [66]	454		442	108		132	80	33	
Pnnm-FeB_4	theor. [67]	408	754	448	219	141	229	165	160	154
	theor. [68]	405	749	479	218	177	225	142	152	129
	theor. [13]	381	710	435	218	114	227	137	143	128
Immm-CrB_4	theor. [13]	591	931	467	252	280	225	64	115	97
	theor. [69]	586	942	519	251	282	227	66	133	
$P2_1/c$-MnB_4	theor. [70]	522	872	524	234	193	222	90	86	96
*Amm*2-ZrB_4	theor. [23]	554	576	454	223	243	254	50	113	122
*C*2/*m*-TaB_4	theor. [27]	497	571	530	242	238	210	139	130	97

Preprints (www.preprints.org) | NOT PEER-REVIEWED | Posted: 12 January 2017 doi:10.20944/preprints201701.0063.v1

Table 2. The calculated bulk modulus *B* (GPa), EOS Fitted Bulk Modulus B_0 (GPa), shear modulus *G* (GPa), Young's modulus *E* (GPa), *G*/*B*, and Poisson's ratio *v*, Debye temperature Θ_D (K), and hardness H_v (GPa) for HfB_4.

structure	work	*B*	B_0	*G*	*E*	*G*/*B*	*v*	Θ_D	H_v
Cmcm-HfB_4	this work	243	244	240	542	0.987	0.128	845	45.7
Fm-3*m*-HfB	this work	173	172	100	252	0.578	0.257	415	12.6
	theor. [39]	252		50	140		0.408		
	theor. [40]	179.7		90.5	232.5	0.504	0.284		13.7
Pnma-HfB	this work	199	197	166	389	0.833	0.173	522	29.2
	theor. [40]	231.1		177.7	424.3	0.769	0.194		26.8
*P*6/*mmm*-HfB_2	this work	253	253	246	558	0.971	0.133	713	45.5
	theor. [43]	278.8		239.5	558.6	0.859	0.166		
	theor. [44]	265	265	240	554	0.906	0.152	698	30.71
	theor. [45]	263		249		0.947	0.14		
	expt. [46]			228	509.9	1.084	0.118	690	
	expt. [47]								31.5
Fm-3*m*-HfB_{12}	this work	236	238	187	444	0.792	0.186	1006	29.5
	theor. [48]	249.5		198.6	470.8	0.796	0.19		39.1
Fm-3*m*-ZrB_{12}	theor. [63]	231.7		193	453.1	0.833	0.174	1206	
	theor. [64]	222		202	466	0.91	0.15	1231	35.4
	expt. [65]	234					0.226	1260	
*P*4/*mbm*-YB_4	theor. [66]	182		144	342	0.791	0.18	874	17.04
	expt. [8]	185.4							
Pnnm-FeB_4	theor. [67]	277	266	186	456	0.671	0.226	1089	
	theor. [68]	263	246	199	476	0.755	0.198	1022.4	
	theor. [13]	253		177		0.697	0.216		24.2
	expt. [12]		252(5)						62(5)
Immm-CrB_4	theor. [13]	275		259		0.942	0.142		45.1
	theor. [69]	290	273	296		1.02	0.119		
	expt. [14]	232(6)							30
$P2_1/c$-MnB_4	theor. [70]	266		235	544		0.159		38.7
	expt. [11]		254(9)						34.6−37.4
*Amm*2-ZrB_4	theor. [23]	241		229	522	0.95	0.139		42.6
*C*2/*m* -TaB_4	theor. [27]	259		220	515	0.855	0.17		29

Preprints (www.preprints.org) | NOT PEER-REVIEWED | Posted: 12 January 2017 doi:10.20944/preprints201701.0063.v1

Figures and Captions

Figure 1. (color online) (a) Crystal structure and polyhedral view of the *Cmcm*-HfB_4 structure. (b) HfB_{12}. Large and small spheres denote Hf and B atoms, respectively.

Figure 2. (color online) Total energy versus f.u. volume for HfB_4 with six different structures.

Figure 3. (color online) Dependence of the formation enthalpy for HfB_4 on the pressure.

Figure 4. Phonon dispersion curves of the *Cmcm*-HfB_4 at 0 GPa (a) and 50 GPa (b).

Figure 5. (color online) Calculated volume compressions as a function of pressure for the HfB_4 compared with HfB, HfB_2, HfB_{12}, *c*-BN, and Diamond.

Figure 6. Three-dimension surface representations of the Young's modulus (a) and bulk modulus (c) for the *Cmcm*-HfB_4. The plane projections of the directional dependence of the Young's modulus (b) and bulk modulus (d) for the *Cmcm*-HfB_4.

Figure 7. (color online) Directional dependences of Young's modulus (a) and the shear modulus (b) in the (100), (010), (001), and $(1\bar{1}0)$ planes.

Figure 8. (color online) Total and partial densities of states of the *Cmcm*-HfB_4. The vertical dashed line denotes the Fermi level E_F.

Figure 9. Contours of ELF of the *Cmcm*-HfB_4 on the (001) (a) and $(10\bar{1})$ (b) plane at 0 GPa.

Preprints (www.preprints.org) | NOT PEER-REVIEWED | Posted: 12 January 2017 doi:10.20944/preprints201701.0063.v1

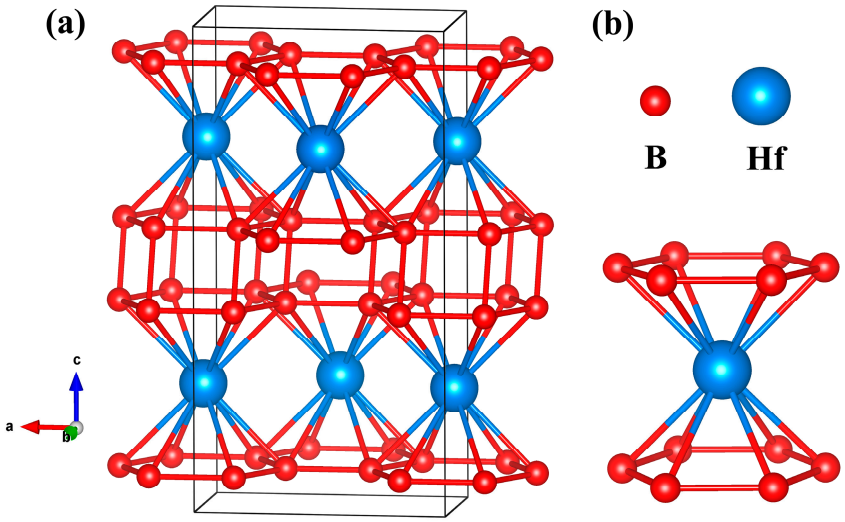

Figure 1

Preprints (www.preprints.org) | NOT PEER-REVIEWED | Posted: 12 January 2017 doi:10.20944/preprints201701.0063.v1

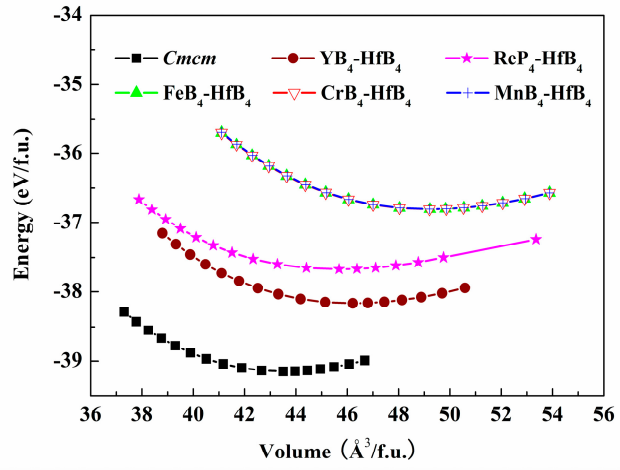

Figure 2

Preprints (www.preprints.org) | NOT PEER-REVIEWED | Posted: 12 January 2017 doi:10.20944/preprints201701.0063.v1

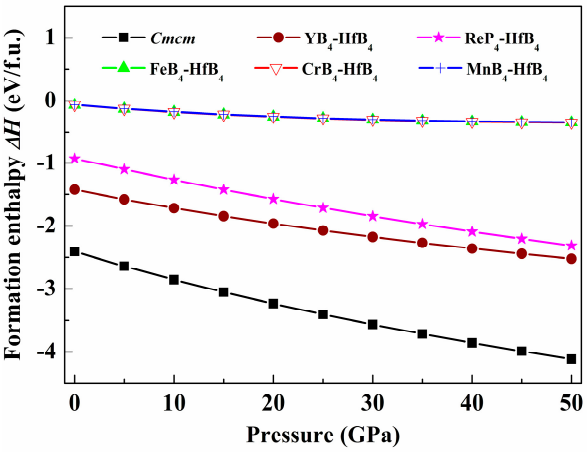

Figure 3

Preprints (www.preprints.org) | NOT PEER-REVIEWED | Posted: 12 January 2017 doi:10.20944/preprints201701.0063.v1

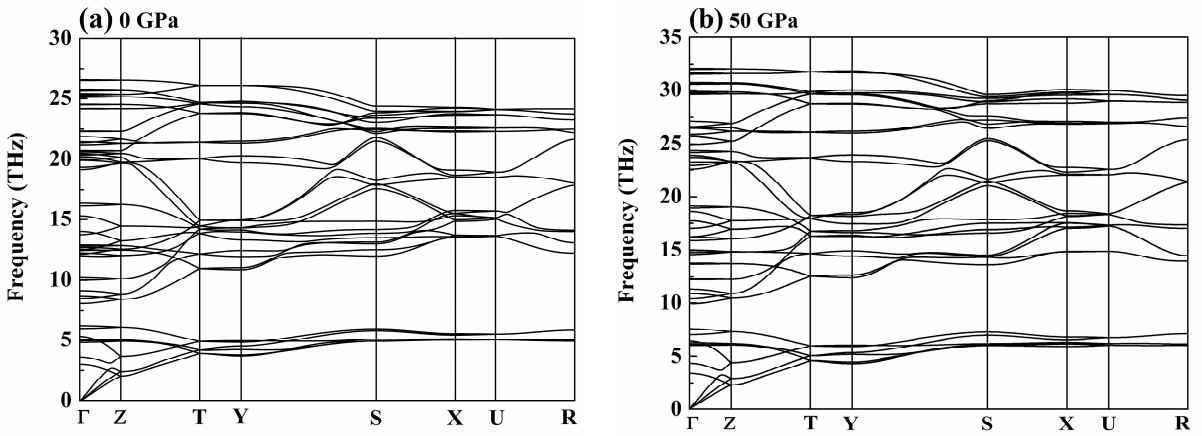

Figure 4

Preprints (www.preprints.org) | NOT PEER-REVIEWED | Posted: 12 January 2017 doi:10.20944/preprints201701.0063.v1

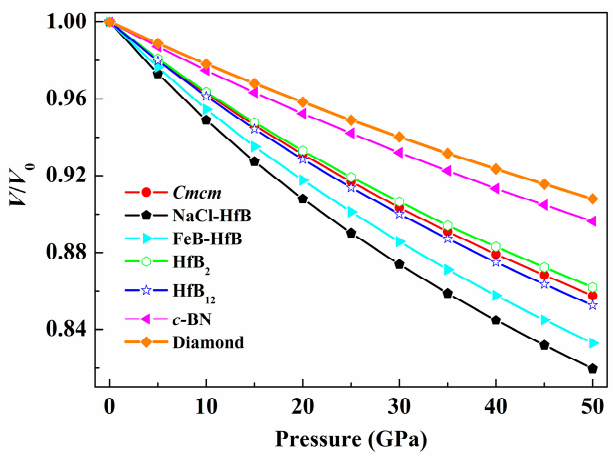

Figure 5

Preprints (www.preprints.org) | NOT PEER-REVIEWED | Posted: 12 January 2017 doi:10.20944/preprints201701.0063.v1

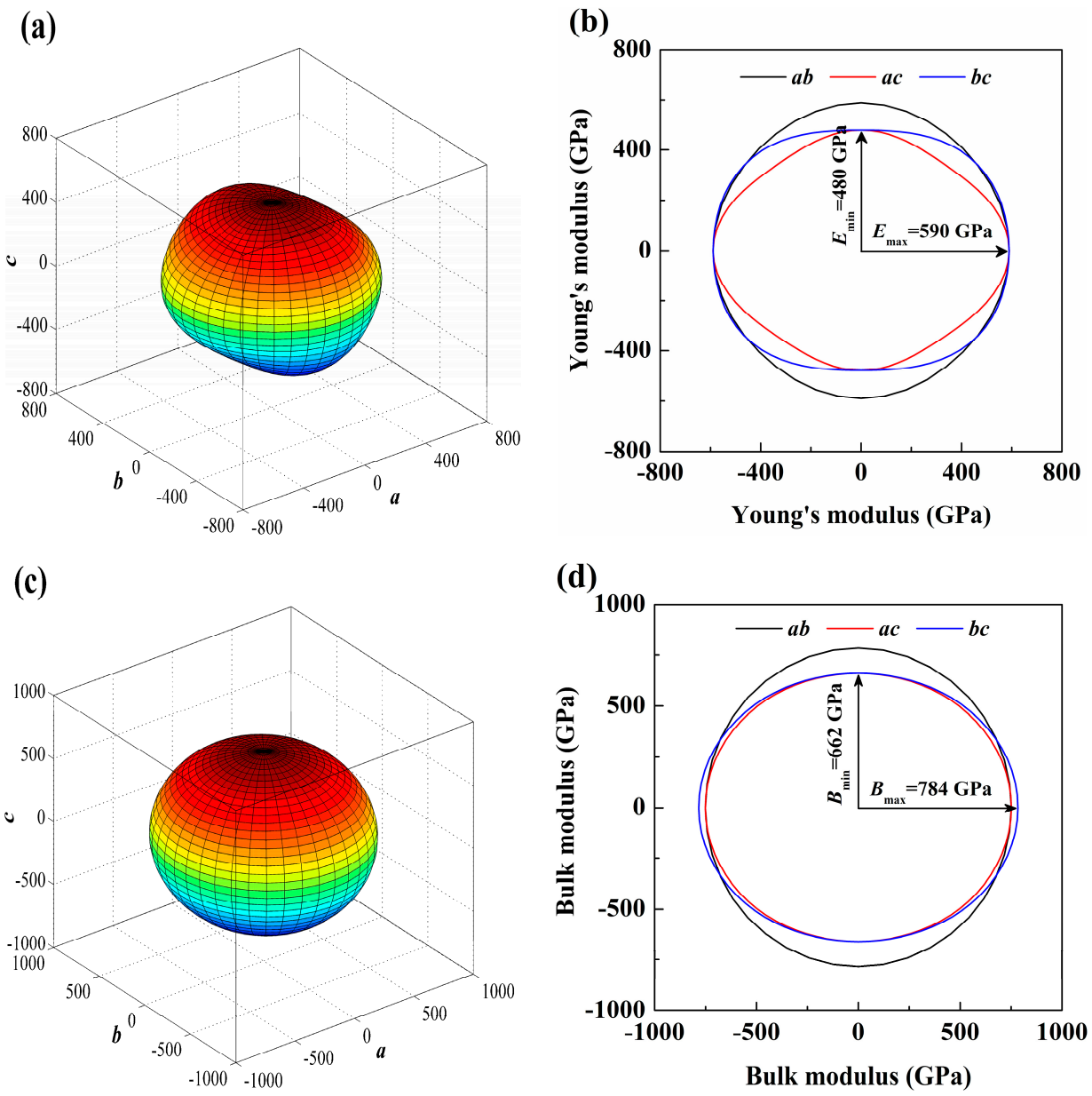

Figure 6

Preprints (www.preprints.org) | NOT PEER-REVIEWED | Posted: 12 January 2017 doi:10.20944/preprints201701.0063.v1

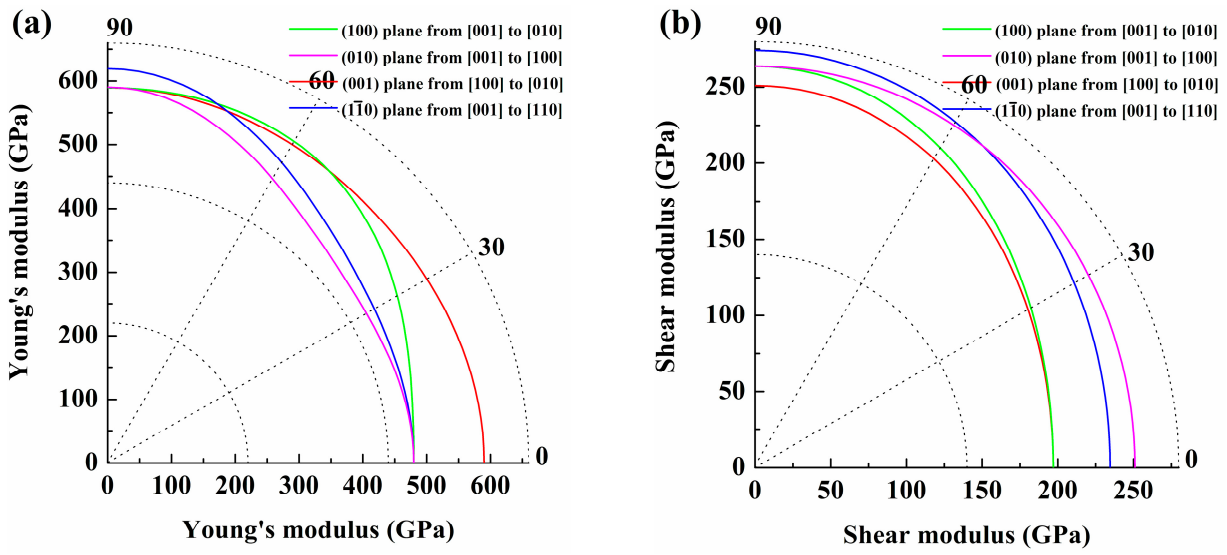

Figure 7

Preprints (www.preprints.org) | NOT PEER-REVIEWED | Posted: 12 January 2017 doi:10.20944/preprints201701.0063.v1

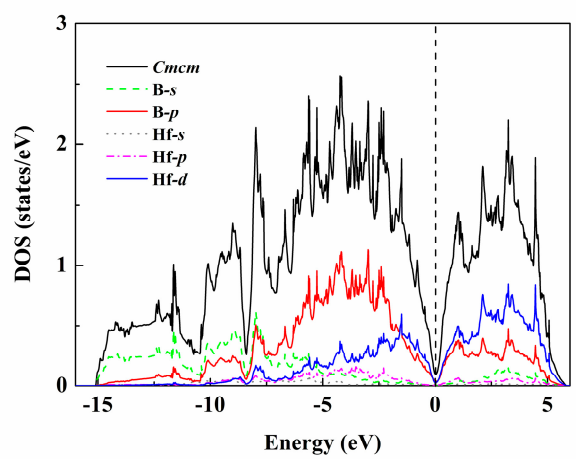

Figure 8

Preprints (www.preprints.org) | NOT PEER-REVIEWED | Posted: 12 January 2017 doi:10.20944/preprints201701.0063.v1